Metal-insulator transition in organic ion intercalated VSe$_2$ induced by dimensional crossover

F. B. Meng,[1] Z. Liu,[1] L. X. Yang,[2] M. Z. Shi,[1] B. H. Ge,[3,4] H. Zhang,[3] J. J. Ying ![ORCID],[1] Z. F. Wang,[1]
Z. Y. Wang,[1] T. Wu,[1,5,7] and X. H. Chen ![ORCID][1,5,6,7,*]

[1]*Hefei National Laboratory for Physical Sciences at Microscale and Department of Physics,*
and CAS Key Laboratory of Strongly-coupled Quantum Matter Physics,
University of Science and Technology of China, Hefei, Anhui 230026, China
[2]*Beijing National Laboratory for Condensed Matter Physics, Institute of Physics, Chinese Academy of Sciences, Beijing 100190, China*
[3]*Institutes of Physical Science and Information Technology, Anhui University, Hefei 230601, China*
[4]*Key Laboratory of Structure and Functional Regulation of Hybrid Materials (Anhui University),*
Ministry of Education, Hefei 230601, China
[5]*CAS Center for Excellence in Superconducting Electronics (CENSE), Shanghai 200050, China*
[6]*CAS Center for Excellence in Quantum Information and Quantum Physics, Hefei, Anhui 230026, China*
[7]*Collaborative Innovation Center of Advanced Microstructures, Nanjing University, Nanjing 210093, China*

The charge-density wave (CDW) transition has been extensively studied in transition metal dichalcogenides (TMDs), the underlying mechanism and the related metal-insulator transition are not as simple as Peierls instability in one dimension and still under hot debate. Here, through electrochemical intercalation of organic ions, we have observed a dimensional crossover induced metal-insulator transition in an organic ion intercalated TMDs: $(TBA)_{0.3}VSe_2$. In pristine VSe$_2$, previous studies have revealed a three-dimensional CDW transition at $T_{CDW} \sim 110$ K with a metallic ground state. After intercalation of organic ions, the remarkable anisotropy of resistivity indicates a highly two-dimensional electronic state in $(TBA)_{0.3}VSe_2$, which is consistent with our density functional theory (DFT) calculation. Interestingly, the dimensional crossover enhances the CDW transition with T_{CDW} of 165 K and leads to an insulating ground state in $(TBA)_{0.3}VSe_2$. Moreover, a commensurate superstructure with $3a \times 3a$ periodicity is also confirmed in this insulating CDW state. Although the DFT calculation suggests that the commensurate superstructure and the enhanced CDW temperature could be ascribed to the improved Fermi surface nesting, whether the metal-insulator transition is driven by a perfect Fermi surface nesting is still elusive at the present stage. The possible role of electronic correlation and electron-phonon coupling has also been discussed. Our work provides a different material platform to study the metal-insulator transition in TMDs.

I. INTRODUCTION

Transition-metal dichalcogenides (TMDs) at the two-dimensional (2D) limit are recently attracting particular interest for their wide varieties of properties [1–5]. TMDs are a series of materials with strong in-plane bonding and weak out-of-plane interactions, and can be easily exfoliated or intercalated [6–8]. These materials usually exhibit various electronic instabilities and tend to form different collectively ordered ground states such as charge density wave (CDW), superconductivity and orbital order [9–11]. Especially, various CDW states in TMDs, such as the incommensurate CDW state in 2H-NbSe$_2$ [12] and the Star-of-David clusters in 1T-TaS$_2$ [13], still draw tremendous interest due to the rich physical phenomenon [14,15]. In principle, the CDW transition can be driven by Peierls instability, in which Fermi surface nesting is the driving force [16]. However, this picture seems to be too simple to explain the complicated CDW states in TMDs, especially for the insulating CDW state in 1T-TaS$_2$ [9,17]. Other

possibilities including q-dependent electron-phonon coupling and electron-electron interaction should be taken into account for the underlying mechanism [18], but there is still a lack of consensus in the community.

Vanadium diselenide (VSe$_2$) is an intriguing member of the TMDs family. In 1T-VSe$_2$, vanadium (V) atoms are sandwiched between two selenium (Se) atomic layers with an octahedral coordination. Bulk crystal of VSe$_2$ exhibits a three-dimensional (3D) CDW phase with $4a \times 4a \times 3c$ period below $T_{CDW} \sim 110$ K [19–23]. Although recent angle-resolved photoemission spectroscopy (ARPES) studies suggested a Fermi surface nesting picture as the mechanism for above 3D CDW state [22,23], the earlier experiments and the recent calculations also suggested an important role of electron-phonon coupling, which is strongly affected by Coulomb repulsion interaction [24–26]. Very recently, further calculations suggested that both Fermi-surface nesting and electron-phonon coupling should account for the 3D CDW state in the bulk 1T-VSe$_2$ [27]. However, other research presented a different viewpoint, which suggested that the Fermi surface of 1T-VSe$_2$ is poorly nested [28]. On the other hand, to further the CDW state in 1T-VSe$_2$, there are more and more

*chenxh@ustc.edu.cn

studies of low-dimensional materials. Through mechanical exfoliation, a dimensional crossover from 3D to 2D leads to an intriguing but highly debated thickness-dependent variation of T_{CDW}. Approaching the dimensional crossover, T_{CDW} firstly decreases with reducing the thickness [29]. When the thickness is below 10 nm, T_{CDW} suddenly increases and finally reaches 130 K in the 2D limit [30]. Recently, a renewed interest in VSe$_2$ is stimulated by the successful preparation of high-quality monolayer thin film with molecular beam epitaxy technique. In these single layer thin films, much higher CDW transition temperatures and different types of commensurate superstructures have been reported [31–33]. Interestingly, ARPES experiments claim a possible insulating state below T_{CDW} with pseudogap features above T_{CDW} in the single layer VSe$_2$ thin film [34]. The aforementioned results suggest different properties of VSe$_2$ in the 2D limit, especially for the insulating CDW state, which deserves further investigation. However, the single layer VSe$_2$ thin films grown are rather unstable, which limits more detailed studies, such as resistivity, specific heat, and magnetic susceptibility measurements.

On the other hand, the dimensional crossover in layered materials could also be achieved by intercalating extra ions into the van der Waals gaps since intercalation can efficiently weaken the interlayer coupling [35,36]. Recent reports have shown that, after inserting SnSe/PbSe between the adjacent VSe$_2$ layers, 1T-VSe$_2$ exhibits a weak insulating behavior below T_{CDW} [37,38]. Organic ions can dramatically increase the spacing between neighboring layers due to their larger volume, which is beneficial to induce dimensional crossover in layered materials. In this work, we successfully obtained organic ion intercalated VSe$_2$ via the electrochemical intercalation of tetrabutyl ammonium (TBA$^+$) - (TBA)$_{0.3}$VSe$_2$. The strong anisotropic resistivity indicates a highly 2D electronic state in (TBA)$_{0.3}$VSe$_2$ which is consistent with our DFT calculation. It strongly suggests a dimensional crossover from 3D to 2D due to the intercalation of organic ions. Interestingly, we also found an enhanced CDW transition temperature of 165 K and an insulating ground states that might share a similar mechanism as the insulating CDW state in the single layer VSe$_2$ thin film [34]. In addition, a commensurate superstructure with $3a \times 3a$ periodicity is also confirmed in the insulating state, in contrast to the $(4 \times 4 \times 3)$ CDW in the bulk material. Our DFT calculation indicates that the superstructure and higher CDW temperature could be ascribed to the improved Fermi surface nesting. However, whether the metal-insulator transition is driven by a perfect Fermi surface nesting is still elusive so far, and the van Hove singularity near the Fermi level may also play an important role here.

II. METHODS

Synthesis of VSe$_2$ *single crystal.* The high-quality VSe$_2$ single crystals were synthesized using the chemical vapor transport (CVT) method, which is similar to the previously reports [39,40]. High purity vanadium (V) powder (Aladdin, 99.5%, 325 mesh) and Selenium (Se) powder (Aladdin, 99.999%, 80 mesh) were mixed with the mole ratio of 1:3, which were then thoroughly grounded. Excess Se powder was taken as the transport segment to simultaneously reduce the Se defect in VSe$_2$ single crystal. Then the mixture was sealed

in a quartz ampoule under high vacuum. The sealed ampoule was placed into a two-zone horizontal furnace with the hot part at about 850 °C and the cold part at about 750 °C for 7 days. The high-quality VSe$_2$ single crystals were obtained at the cold end. The typical size of VSe$_2$ single crystal is 10 mm $\times$ 10 mm $\times$ 0.03 mm.

Electrochemical intercalation of VSe$_2$ *with* TBA$^+$. The VSe$_2$ single crystals were cut into rectangular pieces prior to the electrochemical intercalation. The mass of each single crystal was accurately weighed through a microgram balance (Mettler Toledo AX26). Then the cut VSe$_2$ single crystals were pressed onto an indium wire that was applied as the positive electrode. A silver slice was applied both as the counter electrode and reference electrode. The solution of 4 g tetrabutyl ammonium bromide pieces (TBAB, Aladdin, AR, 99.0%) dissolved into 20 mL N, N-dimethylformamide (DMF, Innochem, 99.9%, extra dry with molecular sieves, water less than 50 ppm) was taken as the electrolyte. The electrolyte cells with the aforementioned electrodes were placed into argon gas glove box. In order for uniform intercalation, a constant current of 20 μA was applied to pass through the electrolytic cell. During the whole electrochemical intercalation process, electrons were lost in negative electrode of Ag pieces, while VSe$_2$ single crystal as positive electrode captured electrons. The amount of intercalation of TBA$^+$ ions in this report was determined as 0.3 according to the discharge curve with the integral of current over time. A detailed explanation is described in Appendix A.

Then, the obtained products were dried in the argon glove box at room temperature for 12 h. The intercalated samples were stored in a sealed plastic bag due to the sensitivity of intercalated samples in air and moisture.

Characterizations of the (TBA)$_{0.3}$VSe$_2$. The x-ray diffraction (XRD) patterns of pristine and intercalated samples were collected using a powder x-ray diffractometer (SmartLab-9, Rigaku Corp.) equipped with Cu Kα radiation and a fixed graphite monochromator. The cross-section transmission electron microscopy (TEM) images of (TBA)$_x$VSe$_2$ and VSe$_2$ single crystal were obtained by a H7700 microscope at 100 kV. The magnetic susceptibility measurement was performed on a magnetic property measurement system (Quantum Design). The resistivity with the standard four-terminal method and specific heat measurements were conducted by a physical properties measurement system (Quantum Design). To avoid the damage from air and moisture, the preparation for transport and specific heat measurements was made in a glove box. Electron diffraction images were obtained using a JEOL-2100 microscope equipped with liquid nitrogen low temperature sample holder at 200 kV.

Theoretical calculation. DFT calculations was performed using the Vienna *ab initio* simulation package with a plane-wave basis set. Also, the projector augmented wave method was applied in conjugation with a generalized gradient approximation (GGA) of exchange-correlation function in the Perdew, Burke, and Ernzerhof functional. For geometric optimization and electronic properties calculation, a plane-wave cutoff of 400 eV was performed. The energy convergence criteria was set at 10^{-6} eV, and the residual force was 0.01 eV/Å. The partial occupations of eigenstates were determined by means of the first-order Methfessel-Paxton smearing with
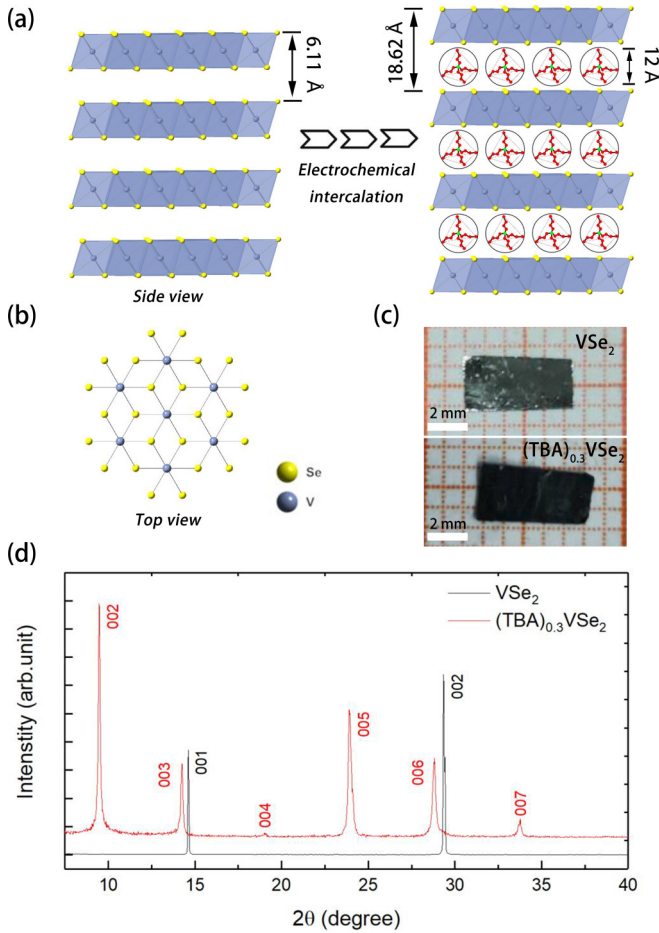
FIG. 1. The structure of pristine VSe_2 and $(TBA)_{0.3}VSe_2$. (a) The side view for structure of pristine VSe_2 and $(TBA)_{0.3}VSe_2$. (b) The top view for structure of pristine VSe_2. (c) The optical images of pristine VSe_2 and $(TBA)_{0.3}VSe_2$. (d) The x-ray diffraction patterns for pristine VSe_2 and $(TBA)_{0.3}VSe_2$, showing a series of (00l) diffraction peaks.

$\sigma = 0.05$ eV. The Brillouin zone integration was carried out through $15 \times 15 \times 1$ k-point sampling for both structure optimization and electronic calculation.

III. RESULTS

High-quality $1T$-VSe_2 single crystals were used as starting material to synthesize $(TBA)_{0.3}VSe_2$ samples. The crystal structure of pristine VSe_2 is shown in Figs. 1(a) and 1(b). For pristine VSe_2, the distance between adjacent layers is 6.11 Å, being consistent with the c-axis parameter of VSe_2 [41]. Figure 1(c) shows optical images of the pristine VSe_2 single crystal and its intercalated product. A direct comparison shows that the $(TBA)_{0.3}VSe_2$ sample almost maintains the same ab-plane size and morphology of the pristine VSe_2 crystal, but becomes much thicker along the c axis, indicating the intercalation of TBA^+ ion. The XRD pattern of $(TBA)_{0.3}VSe_2$ in Fig. 1(d) shows a series of (00l) peaks after intercalation, which can be indexed with a c-axis parameter of 18.62 Å (red line). Given that the size of TBA^+ ion is 8.4–12 Å depending on their orientation (see Fig. 6 in Appendix B), the c-axis parameter of the intercalated sample can be considered as a
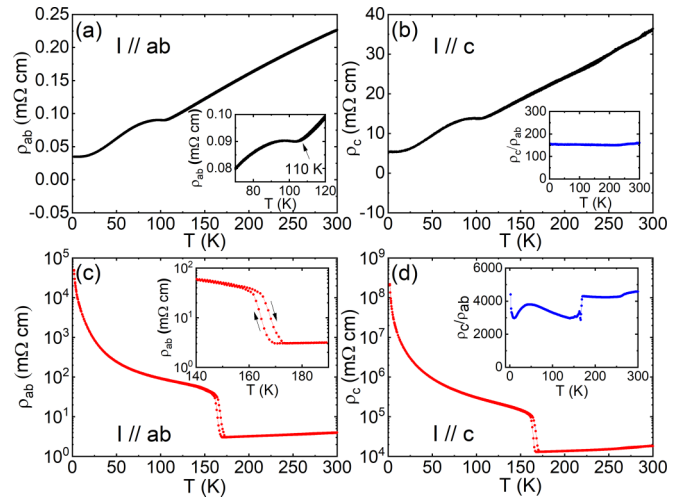
FIG. 2. (a) Temperature dependence of in-plane resistivity for pristine VSe_2. The inset shows the enlarged view of resistivity curve in the vicinity of phase transition for pristine VSe_2. (b) The temperature dependence of out-of-plane resistivity for pristine VSe_2. The inset shows ρ_c/ρ_{ab} versus T for pristine VSe_2. (c) The temperature dependence of in-plane resistivity for $(TBA)_{0.3}VSe_2$. The inset shows the enlarged view of resistivity curve in the vicinity of phase transition for $(TBA)_{0.3}VSe_2$. (d) The temperature dependence of out-of-plane resistivity for $(TBA)_{0.3}VSe_2$. The inset shows ρ_c/ρ_{ab} versus T for $(TBA)_{0.3}VSe_2$. The CDW transition temperature for $(TBA)_{0.3}VSe_2$ is determined by the mean value of middle transition points in cooling and warming curves.

sum of the height of single layer VSe_2 and TBA^+ ion. With all the above information, the crystal structure of intercalated sample is proposed in Fig. 1(a). The huge change of the interlayer spacing between pristine VSe_2 and $(TBA)_{0.3}VSe_2$ are also examined by high resolution transmission electron microscopy (see Fig. 7 in Appendix C). In addition, according to the selected area electron diffraction (SAED) results, the in-plane lattice parameter of $(TBA)_{0.3}VSe_2$ is almost identical to that of the pristine VSe_2 (See Fig. 8 in Appendix D). It should be noted that the TBA^+ ions cannot be observed in the TEM image due to the small diffraction contrast.

Temperature dependence of in-plane and out-of-plane resistivities are measured on both pristine VSe_2 and $(TBA)_{0.3}VSe_2$. As shown in Fig. 2, the in-plane resistivity of pristine VSe_2 shows a metallic behavior with an anomaly around 110 K, which is related to the $(4 \times 4 \times 3)$ CDW transition, being consistent with a previous report [19]. We note that the pristine VSe_2 remains metallic in the 3D CDW state, and no hysteresis around the CDW transition is observed, indicating a second-order phase transition. Furthermore, as shown in the inset of Fig. 2(b), the temperature-dependent anisotropy between in-plane and out-of-plane resistivities shows temperature-independent behavior with a mean value about 150, indicating an anisotropic 3D electronic structure. This is consistent with a 3D Fermi surface revealed by ARPES [23]. In contrast to the pristine VSe_2, the temperature-dependent resistivity of $(TBA)_{0.3}VSe_2$ shows a remarkable metal-insulator transition around 165 K, with a hysteresis upon cooling or warming as can be seen in the inset of Fig. 2(c). This result strongly suggests a first-order
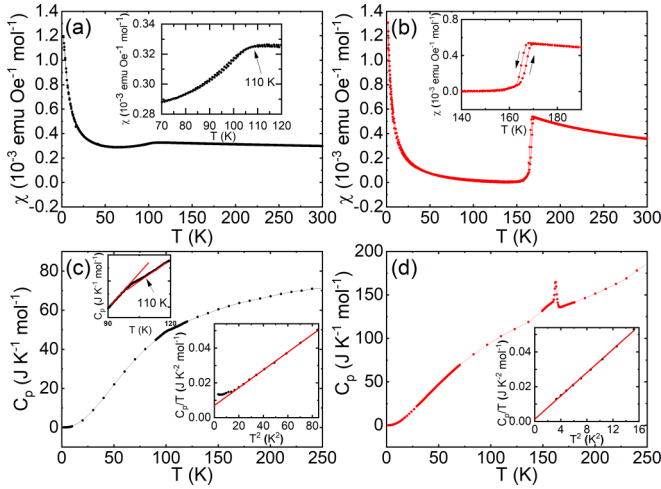
FIG. 3. (a), (b) Temperature dependence of magnetic susceptibility of pristine VSe_2 and $(TBA)_{0.3}VSe_2$ measured at 5 T. The insets show zoom-in of magnetic susceptibility in the vicinity of phase transition. The CDW transition temperature for $(TBA)_{0.3}VSe_2$ is determined by the mean value of middle transition points in cooling and warming curves. (c) The heat capacity of pristine VSe_2. The upper inset shows the enlarged view of heat capacity curve for pristine VSe_2 in temperature range of 90–120 K. The lower inset shows C_p/T as a function of T^2 at low temperature. (d) The heat capacity of $(TBA)_{0.3}VSe_2$. The inset shows C_p/T as a function of T^2 at low temperature. These results definitely indicate that the metal-insulating transition around 165 K for $(TBA)_{0.3}VSe_2$ is a bulk first-order phase transition, while the CDW transition of pristine VSe_2 is second-order.

FIG. 4. The selected area electron diffraction patterns of $(TBA)_{0.3}VSe_2$ along [001] direction at different temperatures. (a) Electron diffraction pattern at 300 K; (b) Electron diffraction pattern at 130 K. The red arrows denote the superstructure diffraction peaks in the CDW state; (c)–(f) Fermi surface topology of VSe_2 with interlayer distance of 6.12, 8.62, 11.02, and 18.62 Å, respectively. (g)–(j) Fermi surface topology with raising Fermi surface by 0.00, 0.05, 0.10, and 0.15 eV at an interlayer distance of 18.62 Å, corresponding nesting vectors are $1/4a^*$, $0.26a^*$, $0.29a^*$, $1/3a^*$ respectively.

metal-insulator transition, which is similar to the Peierls transition in the 1D case. In addition, the anisotropy between in-plane and out-of-plane resistivities has been significantly enhanced by one order of magnitude in the intercalated VSe_2, which supports a highly 2D electronic structure.

To further explore the nature of the metal-insulator transition in the $(TBA)_{0.3}VSe_2$ we have measured the magnetic susceptibility ($\chi = M/H$, where M and H are defined as magnetic moment per mole and magnetic field strength) and specific heat of both the pristine VSe_2 and $(TBA)_{0.3}VSe_2$. The magnetic susceptibility as a function of temperature is measured under magnetic field applied along *ab*-plane direction. For the pristine VSe_2, the magnetic susceptibility is almost temperature independent above 110 K and shows a slight drop below 110 K due to CDW order. At low temperature, the magnetic susceptibility shows a Curie-Weiss-like behavior well below T_{CDW}, which is ascribed to excess V ions in the van der Waals gap between VSe_2 layers (For more details see the Appendix E). For $(TBA)_{0.3}VSe_2$, the magnetic susceptibility shows a clear temperature dependence above 165 K, which might be attributed to a van Hove singularity close to Fermi level. Later in this paper we present more discussion about the van Hove singularity. At about 165 K, the magnetic susceptibility suddenly drops to almost zero value with a hysteresis, which coincides with the metal-insulator transition in resistivity. A Curie-Weiss-like tail below 50 K is also observed in the $(TBA)_{0.3}VSe_2$, which shares the same origin as that in the pristine VSe_2 (See more discussion in Appendix E). As shown in Fig. 3(c), the specific heat measurement on the

pristine VSe_2 shows a weak but noticeable anomaly at T_{CDW} (110 K), which is consistent with a previous report [42]. In the $(TBA)_{0.3}VSe_2$, a first-order transition with a sharp peak is also observed around 165 K, which is consistent with both resistivity and magnetic susceptibility measurements. This result further supports that the metal-insulating transition in the $(TBA)_{0.3}VSe_2$ is a first-order transition. Moreover, compared to the pristine VSe_2, the residual Sommerfeld term (γ) is also significantly reduced in the $(TBA)_{0.3}VSe_2$, as shown in the inset of Figs. 3(c) and 3(d), which suggests a bulk insulating ground state. It should be noted that high temperature ferromagnetism has been predicted by theory calculations [43] and some recent reports have claimed to observe such ferromagnetism at room temperature in a VSe_2 monolayer or thin flakes [44,45]. We have also carried out magnetic field dependent magnetization (*M-H*) measurements to search for ferromagnetism in the $(TBA)_{0.3}VSe_2$. But, unfortunately, no evidence of ferromagnetism is observed in our samples (see Fig. 10 in Appendix F). The absence of ferromagnetism might be related to the strong competition with CDW order [46].

To further characterize the insulating ground state in $(TBA)_{0.3}VSe_2$, we have performed electron diffraction measurements using TEM. Figures 4(a) and 4(b) show the SAED patterns of $(TBA)_{0.3}VSe_2$ along the [001] direction at 300 and 130 K, respectively. For pristine VSe_2, a commensurate $4a \times 4a$ superstructure of the *ab*-plane appears below 110 K, which has been confirmed by previous TEM [47], XRD [41], and
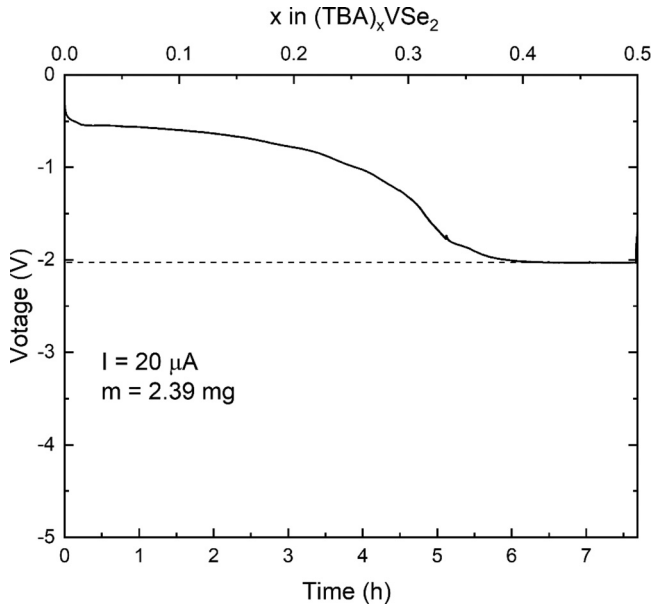
FIG. 5. The discharge curve of $(TBA)_{0.3}VSe_2$ during the electrochemical intercalation process.

scanning tunneling microscope [48] measurements. At room temperature, the electron diffraction pattern of $(TBA)_{0.3}VSe_2$ is similar to that of pristine VSe_2, as shown in Fig. 8 in Appendix D. However, the electron diffraction pattern at 130 K well below the insulating transition temperature shows additional superstructure reflections at (1/3,0,0) [red arrows in Fig. 4(b)]. The superstructure reflections indicate a commensurate CDW modulation with a $3a \times 3a$ periodicity. It suggests that the intercalation of TBA^+ ions leads to an enhanced CDW with a distinct superstructure modulation in VSe_2. In the single layer VSe_2 films, distinct CDW modulations from the bulk VSe_2 have also been reported in previous studies [31–34].

In order to understand the underlying mechanism of the insulating CDW state in the intercalated VSe_2, a preliminary DFT calculation is performed to illustrate the change of band structures and Fermi surface topology with the increase of the interlayer distance. Previous ARPES measurements suggest that the CDW in bulk VSe_2 could be driven by the Fermi surface nesting [22,23]. Considering that the intercalation of organic ions can increase interlayer distance and introduce electron doping, the evolution of band structure and Fermi surface topology under these conditions are calculated. Figures 5(c)–5(f) show the evolution of Fermi surfaces topology with increasing interlayer distance from 6.12 to 18.62 Å [the corresponding band structure is shown in Fig. 11(a) in Appendix G]. As the interlayer distance increases from 6.12 to 18.62 Å, the Fermi surface topology at $k_z = 0.0$ and $k_z = 0.5$ becomes similar with each other. A star-shaped hole pocket at the Γ point and a triangular shape electron pocket at the K point can be recognized. This result suggests that the interlayer coupling becomes weaker with increasing the interlayer distance. Finally, when interlayer distance increases to 18.62 Å, the electronic property of intercalated VSe_2 is similar to that of the monolayer. The nesting vector q_{nest} along a^* stays unchanged, suggesting the CDW would remain a

$4a \times 4a$ pattern if nesting plays a dominated role. This result is also consistent with the phonon calculation shown in Fig. 11(b), which is in accordance with the recent ARPES results [31,34]. In addition, the extra electron doping from the organic ions will lift the Fermi level, which will further modify the topology of Fermi surface. As shown in Figs. 5(g)–5(j), the star-shaped hole pocket at the Γ point shrinks with electron doping, and then completely disappears when Fermi level rises by 0.15 eV (corresponding to $0.3e$ per V atom). Meanwhile, the nesting vector q_{nest} along a^* increase from $1/4a^*$ to $1/3a^*$. In the bulk VSe_2, the 3D Fermi surface nesting will only partly gap out the Fermi surface along the nesting vector and leaves the hole pocket unaffected. Therefore, there are residual electrons at the Fermi level even in the CDW state, which leads to a metallic ground state [22,23]. In $(TBA)_{0.3}VSe_2$, owing to the dimensional crossover and extra electron doping, the Fermi surface nesting becomes stronger, which benefits the stabilization of the CDW state and leads to a fully gapped state with insulating behavior. The nesting vector q_{nest} could explain the superstructure with $3a \times 3a$ periodicity.

IV. DISCUSSION

Although the above discussion based on DFT calculation offers a plausible explanation of the observed metal-insulator transition, there are still some open issues left. As we know, the analysis on the Fermi surface nesting alone is not enough and we need more information on the real part of susceptibility $\chi'(q)$ to determine whether the Fermi surface nesting is or is not the driving force for the CDW transition [49,50]. Usually, the q-dependent electron-phonon coupling also plays a key role in most of CDW transition [17]. Previous research suggested that occupied d bandwidth of VSe_2 is only 0.4 eV [51], which is much narrower than d bandwidth in $1T$-TaS_2 and $1T$-$TaSe_2$ [52]. But Coulomb repulsion between the $3d$ electrons from V is larger than that of $5d$ Ta. According to the Chan and Heine criterion for CDW formation [53], these two cases can account for the relatively weak CDW formation in VSe_2. Electron doping would increase occupied d bandwidth of the narrow V d band of VSe_2, hence increase electron-phonon coupling strength [25]. And the increase of electron-phonon coupling strength can enhance the strength of CDW formation. In our case, considering electron doping from intercalated organic ions, the enhancement of CDW transition temperature may be also induced by increasing the electron-phonon coupling strength upon electron doping. However, the above DFT calculation on the phonon frequency did not find structural instability at the right nesting vector with $q_{nest} = (1/3, 0, 0)$. This also leaves a puzzle for understanding the CDW transition. On the other hand, the temperature dependence in magnetic susceptibility in the $(TBA)_{0.3}VSe_2$ suggests a possible van Hove singularity close to the Fermi level. Usually, the magnetic susceptibility is almost temperature independent in metal. When a van Hove singularity appears close to the Fermi level, we would expect a strong temperature dependence in magnetic susceptibility [54]. In fact, such a van Hove singularity has already been seen in monolayer VSe_2 thin films [31]. If considering the existence of such a van Hove singularity, the hole pocket at
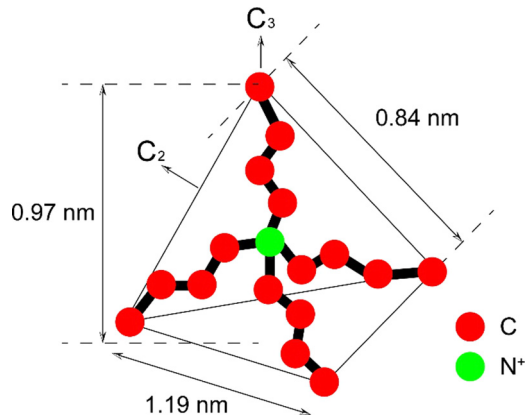
FIG. 6. The schematic structure of tetrabutyl ammonium (TBA$^+$).

Γ point will not sink below the Fermi level in the DFT calculation. Even if we consider a more realistic band structure from a monolayer VSe$_2$ thin film [31], it is also very difficult to understand van Hove singularity with the absence of the hole pocket. Therefore, the existence of a van Hove singularity close to the Fermi level suggests a more complicated mechanism beyond perfect Fermi surface nesting to account for the metal-insulator transition in the (TBA)$_{0.3}$VSe$_2$, which might share similar physics as the cluster Mott insulator in 1T-TaS$_2$ [55–57]. Anyway, our present work provides a different material platform to study the metal-insulator transition in TMDs.

APPENDIX A: ELECTROCHEMICAL INTERCALATION

The electrochemical reaction can be described as the following two reaction equations:

$$\mathrm{Br}^- - e^- + \mathrm{Ag} \rightarrow \mathrm{AgBr} \tag{1}$$

and

$$\mathrm{VSe}_2 + x e^- + x\mathrm{TBA}^+ \rightarrow (\mathrm{TBA})_x \mathrm{VSe}_2. \tag{2}$$
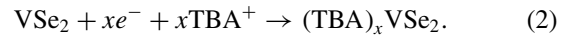
The intercalating amount x of (TBA)$_x$VSe$_2$ can be calculated by the formula below:

$$t = \frac{Fmx}{MI}, \tag{3}$$

where t indicates the time (s), F denotes the faraday constant (96485.31 C/mol), m refers to the mass (g) of the VSe$_2$ single
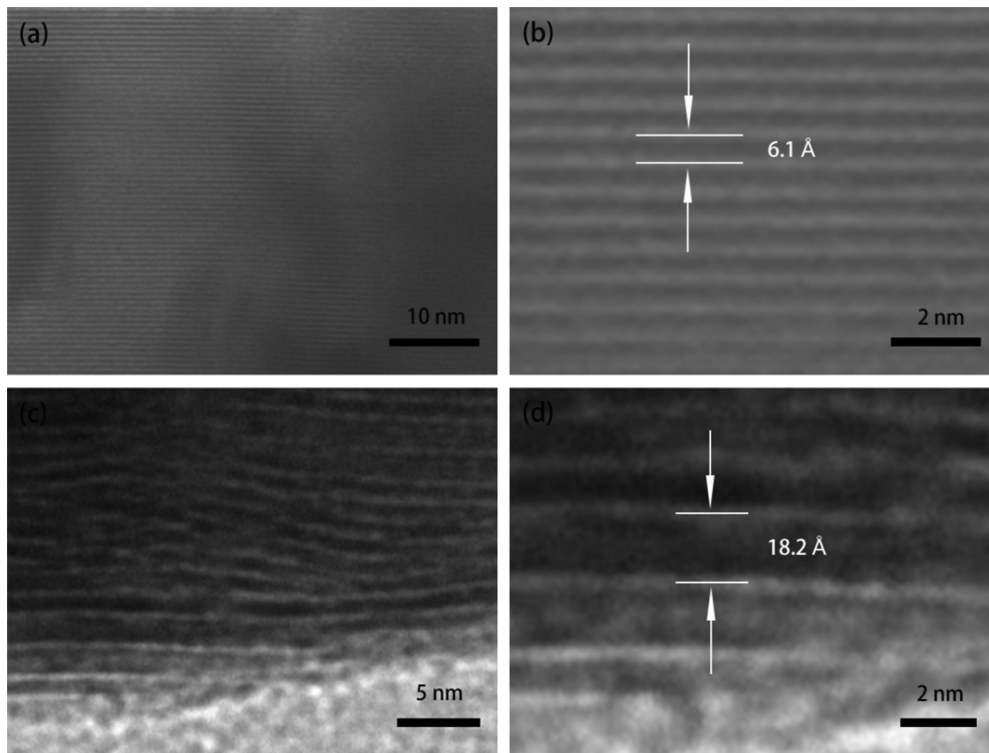
FIG. 7. The cross-section high-resolution TEM images of pristine VSe$_2$ single crystal and (TBA)$_{0.3}$VSe$_2$. (a) The low magnification image of pristine VSe$_2$ single crystal. (b) The high magnification image of pristine VSe$_2$ single crystal. The interlayer spacing of 6.1 Å corresponds to the monolayer height of 1T-VSe$_2$. (c) The low magnification image of (TBA)$_{0.3}$VSe$_2$. (d) The high magnification image of (TBA)$_{0.3}$VSe$_2$. The interlayer spacing is 18.2 Å, which is consistent with the x-ray diffraction results.
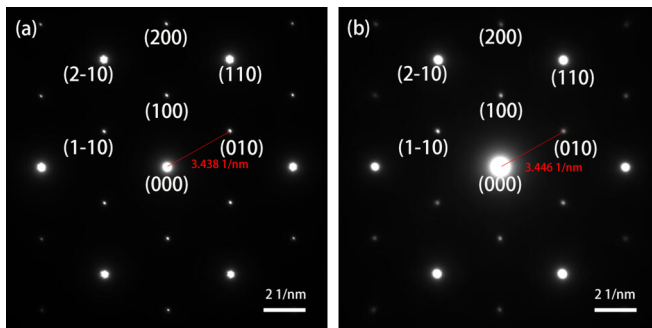
FIG. 8. (a) The in-plane SAED images of pristine VSe_2. (b) The in-plane SAED images of $(TBA)_{0.3}VSe_2$. The SAED results demonstrate that the in-plane lattice parameter of $(TBA)_{0.3}VSe_2$ remains almost the same as pristine VSe_2.

FIG. 9. (a) Temperature dependence of magnetic susceptibility of pristine VSe_2 single crystal measured at 5 T. The red solid line indicates the Curie-Weiss fitting of the susceptibility curves. (b) Temperature dependence of magnetic susceptibility of $(TBA)_{0.3}VSe_2$ measured at 5 Tesla. The red solid line indicates the Curie-Weiss fitting of the susceptibility curves.

crystals, M represents the molar mass (g/mol) of VSe_2, and I stands for the current (A). Herein, the amount of intercalation of TBA^+ ion in this report was determined as 0.3 according to the discharge curve with the integral of current over time, as shown in Fig. 2. The method is usually used to determine the intercalating amount in the process of electrochemical intercalating. As the discharge time was extended, more TBA^+ ions were hindered from intercalation into VSe_2 single crystal by extending discharging time due to the decomposition of electrolyte. However, the unintercalated VSe_2 phase was observed in XRD patterns when $x < 0.3$. The nominal intercalating amount x was made larger than 0.3 in order to obtain pure phase product.

APPENDIX B: THE STRUCTURE OF TBA^+

The schematic diagram of tetrabutyl ammonium ion (TBA^+) [58–60] is shown in Fig. 6. The length in different directions is labeled. Due to TBA^+ intercalation, the increment of interlayer distance is 1.19 nm in the case.

APPENDIX C: THE CROSS-SECTION TEM IMAGINES

To further characterize the structure evolution in the TBA^+ ions intercalation process and confirm the structure of $(TBA)_{0.3}VSe_2$, we performed transmission electron microscopy characterization on pristine VSe_2 and $(TBA)_{0.3}VSe_2$. Figure 7 presents the cross-section TEM images of pristine VSe_2 single crystal and the $(TBA)_{0.3}VSe_2$, respectively. The distance between two adjacent pristine VSe_2 layers is approximately 6.1 Å, which is consistent with the c-axis parameter of VSe_2. The distance between two adjacent VSe_2 layers increases from 6.1 to 18.6 Å due to the intercalation of TBA^+ ion, which is in good agreement with the conclusion from the XRD and the proposed crystal structure. Additionally, as shown in the Figs. 7(c) and 7(d), the intercalation of TBA^+ ions seems to induce disorder. Then, the low temperature magnetic susceptibility of pristine VSe_2 and intercalated $(TBA)_{0.3}VSe_2$ was fitted as shown in Appendix D. Also, it was determined that Curie constant $C = 0.01052$ emu K Oe^{-1} mol^{-1} for pristine VSe_2 and $C = 0.006659$ emu K $Oe^{-1}mol^{-1}$ for $(TBA)_{0.3}VSe_2$. The Curie constant showed no increase after the intercaltion of TBA^+
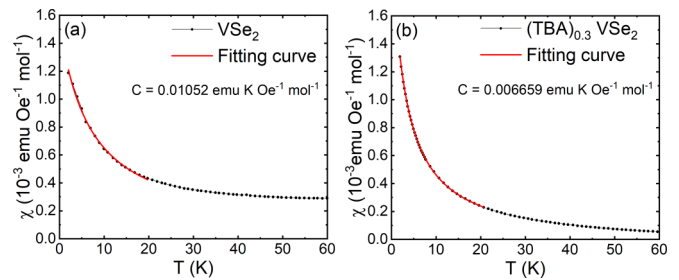
ions, suggesting that the physical effect of disorder induced by the intercalation of TBA^+ ions is not obvious.

APPENDIX D: THE IN-PLANE SAED IMAGES

In order to characterize the variation of in-plane lattice parameter in the TBA^+ ions intercalation process, we performed electron diffraction on pristine VSe_2 single crystal and $(TBA)_{0.3}VSe_2$ in room temperature. Figure 8 shows the in-plane SAED images of pristine VSe_2 and $(TBA)_{0.3}VSe_2$. For the pristine VSe_2, the distance between (010) and (000) is 3.438 1/nm. While for intercalated $(TBA)_{0.3}VSe_2$, the distance between (010) and (000) is 3.446 1/nm. It thus can be known that the difference is merely 0.23%. Therefore, the in-plane lattice parameter of intercalated $(TBA)_{0.3}VSe_2$ remains almost the same as pristine VSe_2, which is in accordance with other organic intercalated compounds such as TaS_2, TiS_2 [61,62].

APPENDIX E: THE CURIE-WEISS FITTING OF THE MAGNETIC SUSCEPTIBILITY

Figure 9 shows the temperature dependence of magnetic susceptibility of pristine VSe_2 single crystal and
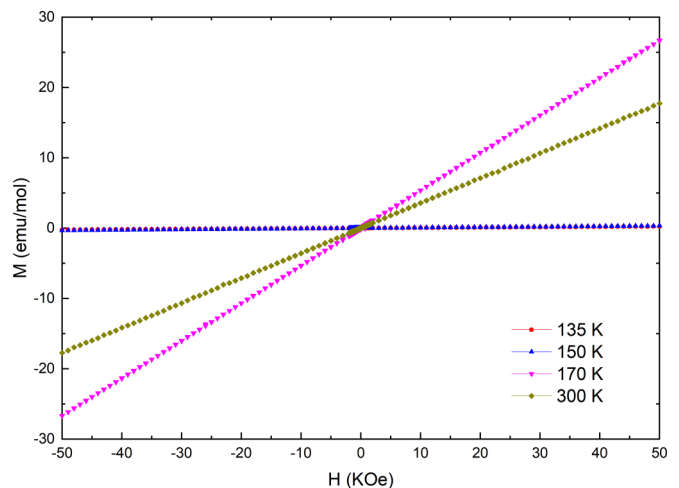
FIG. 10. The magnetic field dependence of magnetic susceptibility (M-H) with $H//ab$ plane for $(TBA)_{0.3}VSe_2$.
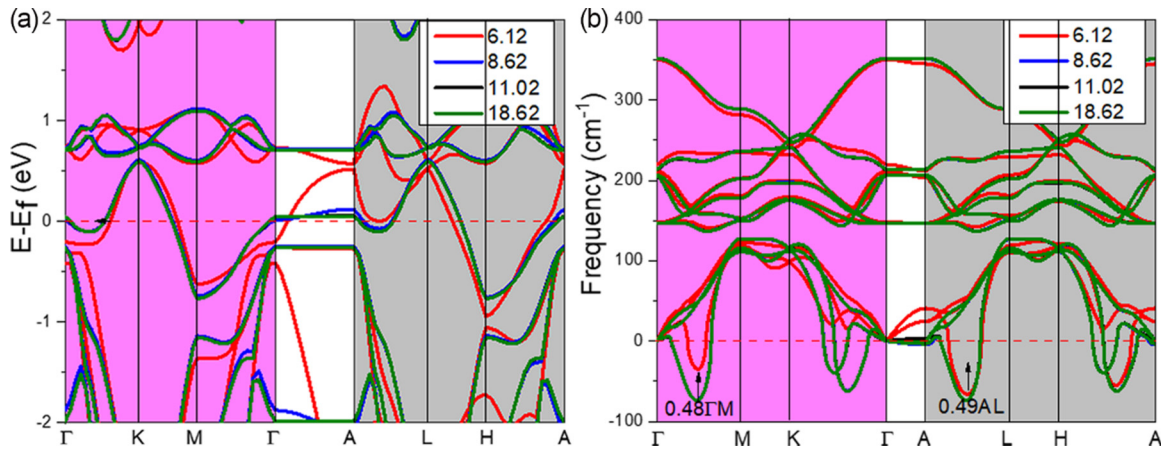
FIG. 11. (a) Band structure and (b) Phonon-dispersion curve of the VSe$_2$ with interlayer distance varying from 6.12 to 18.62 Å.

(TBA)$_{0.3}$VSe$_2$ measured in the temperature range of 2–60 K at 5 T. The magnetic susceptibility manifests a Curie-Weiss-like behavior at low temperature due to excess V ions in the van der Waals gap between VSe$_2$ layers [63,64]. By fitting the data in the temperature range of 2–20 K with Curie-Weiss law $\chi = C/(T - T_{CW}) + \chi_0$ (χ_0 represents a constant), we obtained Curie constant $C = 0.01052$ emu K Oe^{-1}mol^{-1} for pristine VSe$_2$ and $C = 0.006659$ emu K Oe^{-1}mol^{-1} for (TBA)$_{0.3}$VSe$_2$. According to the previous work, each interstitial V ions can produce a net paramagnetic moment of about 2.5 μ_B [63,64]. Basing on this result and the Curie constant obtained, the atomic percentage of the interstitial V ions can be determined to be 1.34% and 0.85% for the pristine VSe$_2$ and (TBA)$_{0.3}$VSe$_2$, respectively.

APPENDIX F: THE MAGNETIC DEPENDENCE OF MAGNETIC SUSCEPTIBILITY

To explore the possible ferromagnetism in intercalated (TBA)$_{0.3}$VSe$_2$, we measured the magnetic field de-

pendent magnetic susceptibility (M-H) on (TBA)$_{0.3}$VSe$_2$. Figure 10 shows the magnetic field dependent magnetic susceptibility of (TBA)$_{0.3}$VSe$_2$ with $H//ab$ plane at different temperatures. (TBA)$_{0.3}$VSe$_2$ exhibits paramagnetism from 300 to 135 K without emergence of ferromagnetism.

APPENDIX G: BAND STRUCTURE AND PHONON DISPERSION

Figure 11(a) shows the band structure of VSe$_2$ with an interlayer distance that differs from 6.12 to 18.62 Å. Figure 11(b) shows the corresponding phonon dispersions of the VSe$_2$. The imaginary frequencies corresponding to soft modes at 1/2 ΓM and 1/2 AL remains unchanged as the interlayer distance increases, suggesting that the change of $4a \times 4a$ superstructure is insignificant when interlayer distance increases.

[1] B. Radisavljevic, A. Radenovic, J. Brivio, V. Giacometti, and A. Kis, Nat. Nanotechnol. **6**, 147 (2011).

[2] Q. H. Wang, K. Kalantar-Zadeh, A. Kis, J. N. Coleman, and M. S. Strano, Nat. Nanotechnol. **7**, 699 (2012).

[3] X. Xi, L. Zhao, Z. Wang, H. Berger, L. Forró, J. Shan, and K. F. Mak, Nat. Nanotechnol. **10**, 765 (2015).

[4] A. H. Castro Neto, Phys. Rev. Lett. **86**, 4382 (2001).

[5] M. M. Ugeda, A. J. Bradley, Y. Zhang, S. Onishi, Y. Chen, W. Ruan, C. Ojeda-Aristizabal, H. Ryu, M. T. Edmonds, H.-Z. Tsaiet, A. Riss, S.-K. Mo, D. H. Lee, A. Zettl, Z. Hussain, Z.-X. Shen, and M. F. Crommie, Nat. Phys. **12**, 92 (2016).

[6] K. S. Novoselov, D. Jiang, F. Schedin, T. J. Booth, V. V. Khotkevich, S. V. Morozov, and A. K. Geim, Proc. Natl. Acad. Sci. U.S.A. **102**, 10451 (2005).

[7] Editorial, Nat. Nanotechnol. **7**, 683 (2012).

[8] N. Liu, P. Kim, J. H. Kim, J. H. Ye, S. Kim, and C. J. Lee, ACS Nano **8**, 6902 (2014).

[9] K. Rossnagel, J. Phys.: Condens. Matter **23**, 213001 (2011).

[10] F. Soto, H. Berger, L. Cabo, C. Carballeira, J. Mosqueira, D. Pavuna, P. Toimil, and F. Vidal, Physica C **460**, 789 (2007).

[11] T. Ritschel, J. Trinckauf, K. Koepernik, B. Büchner, M. V. Zimmermann, H. Berger, Y. I. Joe, P. Abbamonte, and J. Geck, Nat. Phys. **11**, 328 (2015).

[12] D. E. Moncton, J. D. Axe, and F. J. DiSalvo, Phys. Rev. Lett. **34**, 734 (1975).

[13] C. B. Scruby, P. M. Williams, and G. S. Parry, Philos. Mag. **31**, 255 (1975).

[14] S. V. Borisenko, A. A. Kordyuk, A. N. Yaresko, V. B. Zabolotnyy, D. S. Inosov, R. Schuster, B. Büchner, R. Weber, R. Follath, L. Patthey, and H. Berger, Phys. Rev. Lett. **100**, 196402 (2008).

[15] Y. J. Yu, F. Y. Yang, X. F. Lu, Y. J. Yan, Y.-H. Cho, L. G. Ma, X. H. Niu, S. Kim, Y.-W. Son, D. L. Feng, S. Y. Li, S.-W. Cheong, X. H. Chen, and Y. B. Zhang, Nat. Nanotechnol. **10**, 270 (2015).

[16] G. Grüner, Rev. Mod. Phys. **60**, 1129 (1988).

[17] M. D. Johannes and I. I. Mazin, Phys. Rev. B **77**, 165135 (2008).

[18] S. Z. Li, Y. F. Tang, T. A. Maier, and S. Johnston, Phys. Rev. B **97**, 195116 (2018).

[19] M. Bayard and M. J. Sienko, J. Solid State Chem. **19**, 325 (1976).

[20] D. J. Eaglesham, R. L. Withers, and D. M. Bird, J. Phys. C **19**, 359 (1986).

[21] A. M. Woolley and G. Wexler, J. Phys. C **10**, 2601 (1977).

[22] K. Terashima, T. Sato, H. Komatsu, T. Takahashi, N. Maeda, and K. Hayashi, Phys. Rev. B **68**, 155108 (2003).

[23] V. N. Strocov, M. Shi, M. Kobayashi, C. Monney, X. Wang, J. Krempasky, T. Schmitt, L. Patthey, H. Berger, and P. Blaha, Phys. Rev. Lett. **109**, 086401 (2012).

[24] R. H. Friendt, D. Jerome, D. M. Schleich, and P. Molinié, Solid State Commun. **27**, 169 (1978).

[25] M. Sarmat, A. Ghorayeb, S. Nulsen, and R. H. Friend, J. Phys. C **14**, 1055 (1981).

[26] D. M. Zhang, J. Ha, H. Baek, Y.-H. Chan, F. D. Natterer, A. F. Myers, J. D. Schumacher, W. G. Cullen, A. V. Davydov, Y. Kuk, M. Y. Chou, N. B. Zhitenev, and J. A. Stroscio, Phys. Rev. Materials **1**, 024005 (2017).

[27] J. G. Si, W. J. Lu, H. Y. Wu, H. Y. Lv, X. Liang, Q. J. Li, and Y. P. Sun, Phys. Rev. B **101**, 235405 (2020).

[28] J. Henke, F. Flicker, J. Laverock, and J. van Wezel (unpublished).

[29] J. Y. Yang, W. K. Wang, Y Liu, H. F. Du, W Ning, G. Zheng, C. Jin, Y. Y. Han, N. Wang, Z. R. Yang, M. L. Tian, and Y. H. Zhang, Appl. Phys. Lett. **105**, 063109 (2014).

[30] Á. Pásztor, A. Scarfato, C. Barreteau, E. Giannini, and C. Renner, 2D Mater. **4**, 041005 (2018).

[31] J. Feng, D. Biswas, A. Rajan, M. D. Watson, F. Mazzola, O. J. Clark, K. Underwood, I. Markovic, M. McLaren, A. Hunter, D. M. Burn, L. B. Duffy, S. Barua, G. Balakrishnan, F. Bertran, P. Le Fèvre, T. K. Kim, G. van der Laan, T. Hesjedal, P. Wahl, and P. D. C. King, Nano Lett. **18**, 4493 (2018).

[32] G. Duvjir, B. K. Choi, I. Jang, S. Ulstrup, S. Kang, T. T. Ly, S. Kim, Y. H. Choi, C. Jozwiak, A. Bostwick, E. Totenberg, J.-G. Park, R. Sankar, K.-S. Kim, J. Kim, and Y. J. Chang, Nano Lett. **18**, 5432 (2018).

[33] P. Chen, W. W. Pai, Y.-H. Chan, V. Madhavan, M. Y. Chou, S.-K. Mo, A.-V. Fedorov, and T.-C. Chiang, Phys. Rev. Lett. **121**, 196402 (2018).

[34] Y. Umemoto, K. Sugawara, Y. Nakata, T. Takahashi, and T. Sato, Nano Res. **12**, 165 (2019).

[35] H. I. Starnberg, H. E. Brauer, L. J. Holleboom, and H. P. Hughes, Phys. Rev. Lett. **70**, 3111 (1993).

[36] C. Wang, Q. Y. He, U. Halim, Y. Y. Liu, E. B. Zhu, Z. Y. Lin, H. Xiao, X. D. Duan, Z. Y. Feng, R. Cheng, N. O. Weiss, G. J. Ye, Y.-C. Huang, H. Wu, H.-C. Cheng, I. Shakir, L. Liao, X. H. Chen, W. A. Goddard, Y. Huang, and X. F. Duan, Nature (London) **555**, 231 (2018).

[37] M. Falmbigl, A. Fiedler, R. E. Atkins, S. F. Fischer, and D. C. Johnson, Nano Lett. **15**, 943 (2015).

[38] O. K. Hite, M. Falmbigl, M. B. Alemayehu, M. Esters, S. R. Wood, and D. C. Johnson, Chem. Mater. **29**, 5646 (2017).

[39] F. H. Wehmeier, E. T. Keve, and S. C. Abrahams, Inorg. Chem. **9**, 2125 (1970).

[40] C. F. Van Bruggen and C. Hass, Solid State Commun. **20**, 251 (1976).

[41] K. Tsutsumi, Phys. Rev. B **26**, 5756 (1982).

[42] C. S. Yadav and A. K. Rastogi, Solid State Commun. **150**, 648 (2010).

[43] Y. Ma, Y. Dai, M. Guo, C. Niu, Y. Zhu, and B. Huang, ACS Nano **6**, 1695 (2012).

[44] M. Bonilla, S. Kolekar, Y. Ma, H. C. Diaz, V. Kalappattil, R. Das, T. Eggers, H. R. Gutierrez, M.-H. Phan, and M. Batzill, Nat. Nanotechnol. **13**, 289 (2018).

[45] W. Yu, J. Li, T. S. Herng, Z. S Wang, X. X. Zhao, X. Chi, W. Fu, I. Abdelwahab, J. Zhou, J. D. Dan, Z. X. Chen, Z. Chen, Z. J. Li, J. Lu, S. J. Pennycook, Y. P. Feng, J. Ding, and K. P. Loh, Adv. Mater. **31**, 1903779 (2019).

[46] P. M. Coelho, K. N. Cong, M. Bonilla, S. Kolekar, M.-H. Phan, J. Avila, M. C. Asensio, I. I. Oleynik, and M. Batzill, J. Phys. Chem. C **123**, 14089 (2019).

[47] F. Levy, *Crystallography and Crystal Chemistry of Materials with Layered Structure* (Reidel, Dordrecht, Netherlands, 1976), p. 51.

[48] B. Giambattista, C. G. Slough, W. W. McNairy, and R. V. Coleman, Phys. Rev. B **41**, 10082 (1990).

[49] M. D. Johannes, I. I. Mazin, and C. A. Howells, Phys. Rev. B **73**, 205102 (2006).

[50] M. Calandra, I. I. Mazin, and F. Mauri, Phys. Rev. B **80**, 241108(R) (2009).

[51] H. P. Hughes and C. W. A. P. M. Williams, J. Phys. C **13**, 1125 (1980).

[52] N. V. Smith and M. M. Traum, Phys. Rev. B **12**, 2220 (1975).

[53] S.-K Chan and V. Heine, J. Phys. F **3**, 795 (1973).

[54] R. Nourafkan and S. Acheche, Phys. Rev. B **98**, 161116(R) (2018).

[55] L. Perfetti, T. A. Gloor, F. Mila, H. Berger, and M. Grioni, Phys. Rev. B **71**, 153101 (2005).

[56] R. Ang, Y. Tanaka, E. Ieki, K. Nakayama, T. Sato, L. J. Li, W. J. Lu, Y. P. Sun, and T. Takahashi, Phys. Rev. Lett. **109**, 176403 (2012).

[57] L. Perfetti, P. A. Loukakos, M. Lisowski, U. Bovensiepen, H. Berger, S. Biermann, P. S. Cornaglia, A. Georges, and M. Wolf, Phys. Rev. Lett. **97**, 067402 (2006).

[58] Q. M. Gao, O. Giraldo, W. Tong, and S. L. Suib, Chem. Mater. **13**, 778 (2001).

[59] Y. Omomo, T. Sasaki, and L. Wang, and M. Watanabe, J. Am. Chem. Soc. **125**, 3568 (2003).

[60] W. Sugimoto, H. Iwata, Y. Yasunaga, Y. Murakami, and Y. Takasu, Angew. Chem. Int. Ed. **42**, 4092 (2003).

[61] F. R. Gamble, J. H. Osiecki, and F. J. Disalvo, J. Chem. Phys. **55**, 3525 (1971).

[62] H. Boller and H. Blaha, J. Solid State Chem. **45**, 119 (1982).

[63] A. H. Thompson and B. G. Silbernagel, J. Appl. Phys. **49**, 1477 (1978).

[64] A. H. Thompson and B. G. Silbernagel, Phys. Rev. B **19**, 3420 (1979).